

# Localization Errors in MR Spectroscopic Imaging Due to the Drift of the Main Magnetic Field and Their Correction

Assaf Tal\* and Oded Gonen

**Purpose:** To analyze the effect of  $B_0$  field drift on multivoxel MR spectroscopic imaging and to propose an approach for its correction.

**Theory and Methods:** It is shown, both theoretically and in a phantom, that for ~30 min acquisitions a linear  $B_0$  drift (~0.1 ppm/h) will cause localization errors that can reach several voxels (centimeters) in the slower varying phase encoding directions. An efficient and unbiased estimator is proposed for tracking the drift by interleaving short ( $\sim T_2^*$ ), nonlocalized acquisitions on the nonsuppressed water each pulse repetition time, as shown in 10 volunteers at 1.5 and 3 T.

**Results:** The drift is shown to be predominantly linear in both the phantom and volunteers at both fields. The localization errors are observed and quantified in both phantom and volunteers. The unbiased estimator is shown to reliably track the instantaneous frequency in vivo despite only using a small portion of the FID.

**Conclusion:** Contrary to single-voxel MR spectroscopy, where it leads to line broadening, field drift can lead to localization errors in the longer chemical shift imaging experiments. Fortunately, this drift can be obtained at a negligible cost to sequence timing, and corrected for in post processing. **Magn Reson Med 70:895–904, 2013. © 2012 Wiley Periodicals, Inc.**

**Key words:**  $B_0$  drift; field instabilities; chemical shift imaging; localization errors

Temporal instabilities of the spins' resonant frequency have long been recognized as sources of artifacts in various applications ranging from MR spectroscopy to thermometry and fMRI (1–3). Over sufficiently long (many minutes) scans, the resonance frequency undergoes a predominantly linear shift, referred to as field “drift,” due to tiny dissipative losses in the superconducting coil. These are specified in the magnet's data sheets at under 0.1 ppm/h, compared with  $\sim 10^{-3}$  ppm/day of frequency synthesizers (see [programmedtest.com/pts310.html](http://programmedtest.com/pts310.html)). Heating of the passive shims by currents in the active ones is another source of an approximately linear drift (4). Other sources of instability are sequence dependent, such as heating of the magnet's heat shield by fast-switching gradients (5), and physiological, such as respiration, which

introduces a periodic component, often on the order of a sequence's repetition time (TR) (4).

The specific effects of the drift vary, depending on the sequence and total acquisition time, with longer protocols, e.g., fMRI and MR spectroscopic imaging, being the most vulnerable. For EPI-based fMRI, geometric image distortions and ways of correcting them have been reported (6,7). Spatial misregistration that can lead to localization errors can also be incurred with spectrally and spatially selective pulses (8). In single-voxel MR spectroscopy, field drift leads to line broadening which can affect spectral resolution and quantification (9,10). In phase-encoded chemical shift imaging (CSI), however, it can lead to localization errors as previously mentioned, but without detailed analysis of its origins and quantification of its consequences (1,11).

The drift's effects can be removed if the instantaneous frequency is known in each scan, assuming it remains constant throughout a single TR. Several suggestions have been made for monitoring the instantaneous frequency. Some are based on specialized external hardware (12). Others combine drift and motion correction using navigator echoes (6). In fast imaging, the drift has often been estimated from the central k-space point (6,13). As no spatial localization is required, a simple approach involves exciting the water with a (possibly frequency-selective) small tip angle pulse, acquiring a free induction decay (FID), and computing the position of its peak (4,14,15). However, this requires acquiring a full FID, which requires considerable available “dead time” in the sequence. Unless limited by specific absorption rate (SAR), such dead time is best kept to a minimum to reduce total scan time or, alternatively, to improve spatial coverage and signal-to-noise-ratio (SNR) per unit time (16). Three-dimensional (3D) protocols which involve time-multiplexing or multislab acquisitions, and which have little “dead-time” during which a full interleaved FID can be acquired, can be problematic as well (16,17).

In this article, we analyze the effects of a predominantly linear field drift, showing that, unlike single-voxel MR spectroscopy, it does not necessarily broaden spectral lines, but rather introduces localization errors, equivalent to spatial blurring due to a moving filter. To address its effects, we also present a method to obtain the instantaneous resonant frequency at negligible cost in time, by acquiring just the first few milliseconds of the nonlocalized, nonwater-suppressed FID every TR. Then, using a weighted least-squares (WLS) fitting procedure, we obtain an unbiased and efficient estimator for the water frequency: its expectation value matches the true value and it attains the Cramer Rao lower bound, i.e., the smallest possible variance of all possible unbiased estimators.

Department of Radiology, New York University School of Medicine, 660 First Avenue, New York, New York, USA.

Grant sponsor: NIH; Grant numbers: NS050520 and EB01015; Grant sponsor: Human Frontiers Science Project.

\*Correspondence to: Assaf Tal, Ph.D., Department of Radiology, New York University School of Medicine, 660 First Avenue, New York, NY 10016. E-mail: [assaf.tal@nyumc.org](mailto:assaf.tal@nyumc.org)

Received 8 August 2012; revised 1 October 2012; accepted 1 October 2012.

DOI 10.1002/mrm.24536

Published online 19 November 2012 in Wiley Online Library ([wileyonlinelibrary.com](http://wileyonlinelibrary.com)).

© 2012 Wiley Periodicals, Inc.

895

We demonstrate its effectiveness (few tenths of a Hz precision) and the validity of the linear drift approximation in vivo in 10 volunteers at 1.5 and at 3 T.

## THEORY

### $B_0$ Drift Leads to Localization Errors

As shown experimentally below, in vivo drifts are characterized by a dominant linear component, whose effect on the localization of phase-encoded CSI data is demonstrated first in one dimension. The analysis will assume the resonant frequency changes negligibly during the acquisition of a single FID. Although rapid changes within a TR are possible, e.g., due to breathing and blood flow, these are periodic and occur on a fast scale ( $\sim$ seconds) and, therefore, we assume their effect is decoupled from that of the slow, linear decline component of interest.

To obtain  $N$  voxels at a given field-of-view (FOV),  $N$  scans are carried out to sample  $k$ -space at  $N$  equidistant points:  $k_n = -k_{\max}/2 + n\Delta k$  ( $n = 0, 1, \dots, N-1$ ), with  $\Delta k = \text{FOV}^{-1}$  and  $k_{\max} = N\Delta k$ . If a drift of  $\Delta\nu_{\text{scan}}$  Hz accrues between subsequent scans, spaced TR apart, and if the receiver is initially centered on the chemical species in question, then the signal acquired during the  $n$ th scan is:

$$s_n(t) = e^{2\pi i n \Delta\nu_{\text{scan}} t} \int_{-\infty}^{\infty} M_0(x) e^{2\pi i k_n x} dx, \quad [1]$$

where  $M_0(x)$  is the spatial spin density and  $t$  is the intra-scan acquisition time which varies between 0 and  $T_{\text{acq}}$ , on the order of several hundred milliseconds. The signal from the  $m$ th voxel is obtained with an inverse discrete Fourier transform taken over Eq. [1]:

$$\begin{aligned} \hat{s}_m &= \sum_{n=0}^{N-1} s_n e^{-\frac{2\pi i m n}{N}} \\ &= \int_{-\infty}^{\infty} M_0(x) \left\{ \sum_{n=0}^{N-1} e^{2\pi i n \Delta\nu_{\text{scan}} t} e^{2\pi i k_n x} e^{-\frac{2\pi i m n}{N}} \right\} dx. \end{aligned} \quad [2]$$

Carrying out the summation within the curly brackets, we obtain:

$$\hat{s}_m(t) = \int_{-\infty}^{\infty} M_0(x) \text{PSF}(x + \Delta\nu_{\text{scan}} \cdot \text{FOV} \cdot t - m\Delta x) dx, \quad [3]$$

where  $\Delta x = \text{FOV}/N$  is the voxel size and  $\text{PSF}(x)$  is the point spread function associated with the phase encoding process (18):

$$\text{PSF}(x) = e^{-\frac{\pi i x}{\text{FOV}}} \frac{\sin\left[\frac{\pi x}{\Delta x}\right]}{\sin\left[\frac{\pi x}{\text{FOV}}\right]}, \quad [4]$$

i.e., the signal from the  $m$ th voxel is given by a convolution of a PSF and the spin distribution,  $M_0(x)$ . The PSF, however, also shifts during the acquisition, picking up signal from the center of the voxel at  $t = 0$  and shifting linearly up to:

$$\delta_x = \Delta\nu_{\text{scan}} \cdot \text{FOV} \cdot T_{\text{acq}} = \Delta\nu_{\text{scan}} \cdot N_{\text{scans}} \cdot \Delta x \cdot T_{\text{acq}}. \quad [5]$$

Typical parameters (TR = 1 s, 0.1 ppm/h drift at 3 T, FOV = 8 cm,  $N_{\text{scans}} = 8$ ,  $T_{\text{acq}} = 0.5$  s) yield  $\delta \approx 0.1$  mm,

which is small compared to the typical ( $\sim 1$  cm)<sup>3</sup> CSI voxel.

Although negligible in 1D, the effective frequency drift between successive points in  $k$ -space becomes non-negligible in 2D and 3D. Indeed, if one acquires  $k$ -space rectilinearly,

$$\begin{aligned} \mathbf{k}_{\text{pqm}} &= -2^{-1}(k_{\max,x}, k_{\max,y}, k_{\max,z}) + (p\Delta k_x, q\Delta k_y, m\Delta k_z) \\ (p, q, m) &= (0, 0, 0), (1, 0, 0), \dots, (N_x - 1, 0, 0), (0, 1, 0), \\ &\quad \times (1, 1, 0), \dots, (N_x - 1, N_y - 1, N_z - 1), \end{aligned} \quad [6]$$

where  $\Delta k_q = \text{FOV}_q^{-1}$  ( $q = x, y, z$ ), the signal from the  $\mathbf{k}_{\text{pqm}}$  coordinate in  $k$ -space is given by:

$$s_{\text{pqm}}(t) = e^{2\pi i (p+qN_x+mN_xN_y)\Delta\nu_{\text{scan}} t} \int M_0(\mathbf{r}) e^{2\pi i \mathbf{k}_{\text{pqm}} \cdot \mathbf{r}} d\mathbf{r}. \quad [7]$$

Reconstruction by an inverse 3D discrete Fourier transform over all three axes yields:

$$\hat{s}_{\text{pqm}}(t) = \int \left[ \begin{array}{l} M_0(\mathbf{r}) \cdot \text{PSF}(x + \Delta\nu_{\text{scan}} \cdot \text{FOV}_x \cdot t - p\Delta x) \\ \cdot \text{PSF}(y + \Delta\nu_{\text{scan}} \cdot \text{FOV}_y \cdot N_x \cdot t - q\Delta y) \\ \cdot \text{PSF}(z + \Delta\nu_{\text{scan}} \cdot \text{FOV}_z \cdot N_x \cdot N_y \cdot t - m\Delta z) \end{array} \right] d\mathbf{r}. \quad [8]$$

As before,  $M_0(x)$  is convolved with a moving PSF. Note, however, that the shift increases  $N_x$ -fold in the second dimension, and  $N_x \cdot N_y$ -fold in the third, due to longer delays between consecutive  $k$ -space points along these axes. Taking  $N_x = N_y = 16$ ,  $\text{FOV}_z = 40$  mm, the shift along the  $z$ -axis is  $\delta_z = \Delta\nu_{\text{scan}} \cdot \text{FOV}_z \cdot N_x \cdot N_y \cdot T_{\text{acq}} \approx 17$  mm, which approaches  $\text{FOV}_z$  itself. Note that Eq. [3] and its 2D and 3D analogues hold even if spatial filtering is used to smooth the PSF.

### Criterion for Neglecting Drift

The drift's effects can be neglected when the shift it induces is negligible compared to the voxel size. For a 3D CSI, the greatest shift is shown to occur along the slowest  $z$ -axis,  $\delta_z = \Delta\nu_{\text{scan}} \cdot \text{FOV}_z \cdot N_x \cdot N_y \cdot T_{\text{acq}}$ , and the criterion becomes  $\delta_z < \Delta z$ . As  $\text{FOV}_z = \Delta z \cdot N_z$ , and  $N_{\text{scans}} = N_x \cdot N_y \cdot N_z$ , this becomes  $\Delta\nu_{\text{scan}} \cdot N_{\text{scans}} \cdot T_{\text{acq}} < 1$ . As  $T_{\text{acq}}$  is typically of the order of  $T_2^*$  in a voxel, approximately the inverse of the linewidth  $\Delta\nu_{\text{FWHM}}$ —the criterion becomes:

$$\Delta\nu_{\text{scan}} \cdot N_{\text{scans}} \ll \Delta\nu_{\text{FWHM}}, \quad [9]$$

where  $\Delta\nu_{\text{scan}} \cdot N_{\text{scans}}$  is simply the total drift accrued throughout the experiment. Eq. [9] can be derived for 1D and 2D acquisitions as well.

### Frequency Estimation Using WLS

The spins' instantaneous frequency can be monitored by interleaving the CSI scans with a pulse-acquire module. Such a module using a small tip angle—so as not to disturb the magnetization appreciably—will yield an FID dominated by the intense water signal, with some lipids contribution. A single dominant frequency component can be modeled as a decaying exponential embedded in normally distributed noise with a fixed variance,  $\sigma^{(xy)}$ :

$$s_n = s_0 \cdot e^{2\pi i v_0 t_n - \frac{t_n}{T_2}} + \varepsilon_R + i\varepsilon_I, \quad n = 0, 1, \dots, N-1 \quad [10]$$

where  $s_0$  is the SNR at the initial point of the FID,  $t_n = n\Delta t$  and  $\Delta t$  is the acquisition dwell time. In the presence of intermediate-to-high SNR  $\geq 3$ , it is well known that the phase of  $s_n$ ,  $\phi_n = \arctan\left(\frac{\text{Im}(s_n)}{\text{Re}(s_n)}\right)$ , follows a normal distribution with mean  $2\pi v_0 t_n$  and standard deviation  $\sigma_n = \sigma^{(xy)} \cdot s_0^{-1} \cdot \exp(t_n/T_2)$  (19); that is, as  $t_n$  increases, so does the phase's uncertainty. The instantaneous frequency,  $v_0$ , can be estimated from the slope of the phase data  $\phi_n$ . It is known that the optimal estimator for this slope is obtained via WLS, where time point is assigned a weight proportional to its SNR (20):

$$\hat{v} = \frac{1}{2\pi} \left[ \frac{\left( \sum_{n=0}^{N-1} \frac{t_n}{\sigma_n^2} \right) \left( \sum_{n=0}^{N-1} \frac{\phi_n}{\sigma_n^2} \right) - \sum_{n=0}^{N-1} \left( \frac{t_n \phi_n}{\sigma_n^2} \right) \left( \sum_{n=0}^{N-1} \frac{1}{\sigma_n^2} \right)}{\sum_{n=0}^{N-1} \left( \frac{t_n}{\sigma_n} \right)^2 - \sum_{n=0}^{N-1} \left( \frac{t_n^2}{\sigma_n^2} \right) \sum_{n=0}^{N-1} \left( \frac{1}{\sigma_n^2} \right)} \right] \quad [11]$$

which is valid even for non-equispaced time points. It is unbiased, efficient and computationally fast, requiring only addition and multiplication of  $O(N)$  terms. Its standard deviation can be calculated explicitly (20):

$$\text{SD}_{\hat{v}} = \sqrt{\text{Var}(\hat{v})} = \frac{1}{2\pi} \cdot \sqrt{\frac{\sum_{n=0}^{N-1} \frac{1}{\sigma_n^2}}{\sum_{n=0}^{N-1} \left( \frac{t_n^2}{\sigma_n^2} \right) \sum_{n=0}^{N-1} \left( \frac{1}{\sigma_n^2} \right) - \sum_{n=0}^{N-1} \left( \frac{t_n}{\sigma_n} \right)^2}} \quad [12]$$

## METHODS

The experiments were done in a 3 T TIM-Trio and a 1.5 T Avanto full body MR imagers using their standard transmit-receive head-coils, capable of delivering 22  $\mu\text{T}$  (0.9 kHz) of  $\mathbf{B}_1$  (Siemens AG, Erlangen Germany). In vivo experiments were done on 10 (eight males, two females) healthy 22–39 year old volunteers. Each provided institutional review board-approved written consent.

### 3D CSI in a Phantom

To observe the localization artifacts described in Eq. [3], a 3D CSI experiment was conducted at 3 T, on a 1.6 cm diameter sphere containing water. A 3D MPRAGE image was acquired at 1 mm isotropic resolution for image guidance of the CSI grid. The 3D CSI sequence consisted of a 90° excitation, followed by quick (250  $\mu\text{s}$ ) gradient phase encoding along all three axes and a subsequent 1-second FID acquisition of 1024 points, as shown in Figure 1a. Following each acquisition, a small, 1°, flip angle pulse was applied and a second FID (1024 points for 1024 ms) was acquired without any localization to track the water's frequency drift. A total of  $10 \times 10 \times 10$  phase encoding steps were applied along the x, y, and z axes at  $200 \times 200 \times 200 \text{ mm}^3$  FOV, leading to  $2 \times 2 \times 2 \text{ cm}^3$  voxels. The phantom was contained entirely within the central voxel of the FOV (Fig. 2a). k-space was acquired rectilinearly (Eq. [6]), with the z-axis being the "slowest" to change. The TR, which includes the second

drift-tracking acquisition, was 2.2 s, leading to a total acquisition time of  $10 \times 10 \times 10 \times 2.2 \text{ s} \approx 36.6 \text{ min}$ . Strong, random gradients ( $\sim 18 \text{ mT/m}$ ) at the end of each TR spoiled any remaining transverse magnetization.

The acquired 3D CSI FIDs were apodized with a Gaussian and zero-filled to 4096 points in the time domain and Fourier transformed along all four ( $k_x$ - $k_y$ - $k_z$ -time) axes to yield a localized spectrum from each voxel. Automatic zero order phase correction was applied in all voxels.

To estimate the instantaneous frequency, each interleaved nonlocalized FID was zero-filled 16-fold to increase its spectral resolution and then Fourier transformed. The spectral position of the water peak was used as an estimator for the instantaneous frequency which was then plotted as a function of total scan time (36.6 min) and inspected visually for linearity. It was linearly fit,

$$v(t) = \alpha_1 t + \alpha_0. \quad [13]$$

The drift,  $\alpha_1$ , in Hz/h, was then corrected for by multiplying each  $k$ th FID by  $\exp(2\pi i \alpha_1 \tau_k t)$ , where  $\tau_k = k \cdot \text{TR}$  is the time at which it was collected and  $0 \leq t \leq 1024 \text{ ms}$  the analog-to-digital conversion (ADC) time variable.

The correction quality was assessed by visual inspection of the drift-corrected spectra and calculating the total spatial leakage outside the voxel containing the phantom. To do so, the area under the real part of the spectrum was obtained by integrating from  $\pm 20 \text{ Hz}$  about the phased water peak. This yielded a positive number for each voxel,  $L_{ijk}$  ( $i, j, k = 1, \dots, 10$ ). The total leakage was defined as the percentage of signal outside the voxel containing the phantom:

$$L_{\text{total}} = \sum_{i, j, k \neq \text{phantom}} L_{ijk} \bigg/ \sum_{i, j, k=1}^{10} L_{ijk} \cdot 100\%. \quad [14]$$

$L_{\text{total}}$  will be greater than 0 even in a perfect, driftless 3D CSI experiment, due to the nonlocal nature of the PSF (Eq. [4]), and can be calculated by simulating the Bloch equations numerically using the same parameters used in the experiment. The simulation yields  $L_{\text{total}} = 38\%$  in the absence of any drift. Calculating  $L_{\text{total}}$  before and after drift-correction would quantify the effect of the drift and the quality of its correction.

### 2D PRESS-CSI and Drift Correction In Vivo

The frequency drift was tracked in 10 healthy volunteers at 1.5 and 3.0 T to quantify its magnitude in vivo. First, a localizer was run, followed by a 5:26 minute 3D MPRAGE ( $1 \times 1 \times 1 \text{ mm}^3$  resolution and  $256 \times 256 \times 192 \text{ mm}^3$  FOV). Our in-house whole-head shimming routine was then used to perform  $B_0$  shimming in each volunteer in about 5 min (21). This was followed by a 2D PRESS CSI acquisition of a 12-mm thick axial 2D slice in the plane of the superior lateral ventricles and an  $8 \times 8 \text{ cm}^2$  VOI was prescribed in a  $24 \times 24 \text{ cm}^2$  FOV, with a  $N_x \times N_y = 24 \times 24$  acquisition matrix in its plane. With a TR/echo time = 3000/60 ms the total acquisition time was 29 min (including four dummy scans to establish a dynamic equilibrium). The CSI was interleaved with the same 1° tip angle pulse-acquire module described above for the phantom. The instantaneous

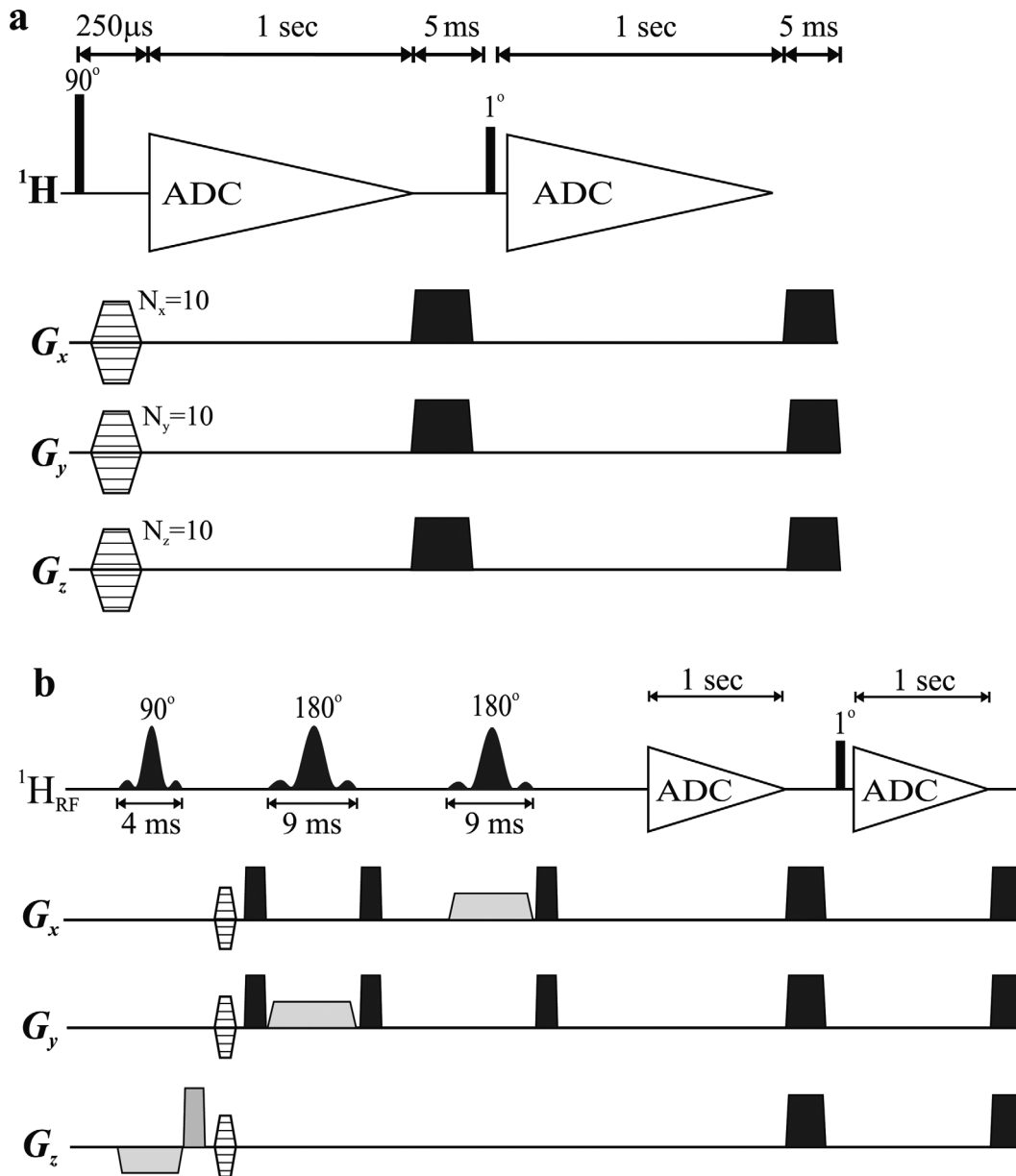


FIG. 1. Pulse sequences used for (a) phantom experiments and (b) in vivo experiments. (a) is 3D CSI, while (b) is 2D CSI PRESS. In both sequences,  $k$ -space was encoded in this order:  $k_x$ - $k_y$ - $k_z$ , i.e., the  $k_x$  coordinate changed every TR,  $k_y$  every  $N_x$ -TR, and  $k_z$  every  $N_x \cdot N_y \cdot \text{TR}$ , as described by Eq. [6]. Both sequences feature an additional interleaved small, 1°, tip-angle pulse-acquire module to track the water signal's instantaneous frequency. The durations of all elements, pulses' bandwidths (at FWHM) and gradients' strengths are marked. Dark gradients represent spoilers/crushers and light-grayed once represent slice/volume selection. The phase encoding gradients, which follow the refocusing gradient in (b), are omitted for brevity.

water frequency was estimated using two approaches: (i) by zero-filling 16-fold (for smoothing), Fourier-transforming, and noting its peak position, and (ii) using the WLS estimator (Eq. [11]) on the initial points of the FID, up until  $T = 10$  ms. The choice of  $T = 10$  ms is made using Eq. [12] as follows: taking  $T_2^* = 10$  ms for a well-shimmed whole-head, a conservative  $s_0/\sigma^{(xy)} = 50$  and a dwell time of 0.5 ms (implying  $N = 21$  points acquired during  $T = 10$  ms), Eq. [12] yields a standard deviation of  $\text{SD}_v = 0.25$  Hz. This is much smaller than the overall drift-induced change in frequency we would expect during the entire scan and hence acceptable. A larger portion of the FID, longer than

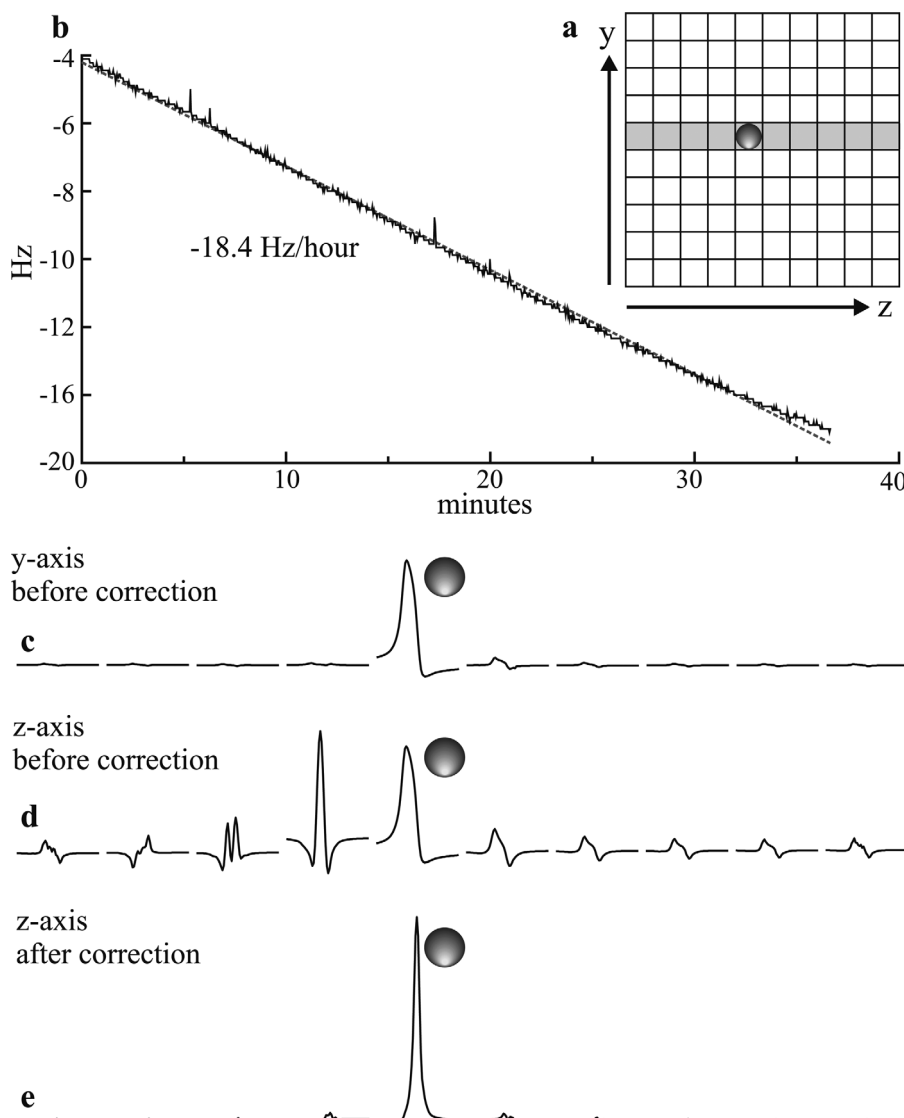
10 ms, can be used to further minimize the standard deviation.

## RESULTS

### 3D CSI in a Phantom

The positioning of the sample and spectroscopic imaging grid is shown in Figure 2a for the ( $yz$ ) slice containing the phantom. The shimmed linewidth was  $3 \pm 1$  Hz. The instantaneous frequency, extracted from the pulse-acquire module interleaved with each CSI scan, is shown in Figure 2b, along with the fitted linear line, which yielded a drift of

FIG. 2. The 3D CSI spectra acquired at 3 T from a homogeneous spherical phantom occupying only the center voxel. **a**: A schematic diagram of the ( $yz$ ) plane containing the phantom and of the placement of the FOV. **b**: The instantaneous frequency as a function of the experiment's duration, as estimated from the pulse-acquire module interleaved with the CSI acquisition. A linear fit yielded a drift of  $-18.4$  Hz/h. **c**: Spectra from the set of voxels containing the phantom along the  $y$ -axis ( $k_y$  is incremented every  $N_x \cdot TR = 30$  s). The voxel containing the phantom is marked by a small sphere. **d**: Spectra from the set of voxels containing the phantom along the "slow"  $z$ -axis ( $k_z$  is incremented every  $N_x \cdot N_y \cdot TR = 300$  s), showing the pronounced effects of drift. **e**: Following correction of the drift, the spectra shown in (d) appear much more symmetrical and well proportioned, and signal becomes mostly confined to the central voxel as expected.



$\alpha_1 = -18.4$  Hz/h =  $-0.15$  ppm/h. The spectra from the set of voxels containing the phantom along the "slowest" varying  $z$ -axis, highlighted in Figure 2a, are shown in Figure 2d. Significant signals outside the main voxel are evident. For comparison, the spectra from the set of voxels containing the phantom along the  $y$ -axis are shown in Figure 2c. These show significantly less artifacts since the time between consecutive points along the  $k_y$ -axis is much shorter (by a factor of  $N_z = 10$ ) than along the  $k_z$ -axis.

The leakage (Eq. [14]) before drift-correction was found to be  $L_{total} = 75\%$ , in contrast to the expected 38% in the absence of drift. The same set of 10 voxels in Figure 2d are shown in Figure 2e after applying the drift correction, using the calculated drift coefficient ( $-18.4$  Hz/h). The corrected spectra display significantly improved localization and spectral quality. The leakage was found to be  $L_{total} = 41\%$ , in better agreement with the theoretically predicted 38%.

### 2D CSI In Vivo

Because of the temporal proximity of the small tip angle excitation and the FID readout, the first 10 points of

each interleaved FID were distorted and were therefore discarded prior to carrying out any frequency estimation. The instantaneous frequency recorded from all 10 volunteers is shown in Figure 3 for both the Fourier-transformed (blue) and WLS (red) estimation, with the WLS estimator using only the first 21 points (10 ms) of the FID. Both estimators show good agreement. Both frequency curves were linearly fitted, with the results displayed in Figure 3 in ppm/h. The average  $\pm$  standard deviation taken over all volunteers of the difference between the two fits is  $0.001 \pm 0.11$  ppm/h. A sample interleaved FID from a single scan from one of the volunteers is shown in Figure 4, alongside the fitted linear curve calculated from the WLS estimator.

Sample in vivo spectra from a volunteer (Fig. 3d) are shown in Figure 5 before and after drift correction. Correction was applied after smoothing the instantaneous frequency curve in Figure 3d and multiplying each PRESS FID by  $\exp(2\pi i \nu_m t)$ , where  $0 \leq t \leq 1024$  ms is the ADC time variable and  $\nu_m$  ( $m = 1, 2, \dots, 576$ ) is the instantaneous frequency during the  $m$ th scan. Voxels adjacent to discontinuities in the spin density along the

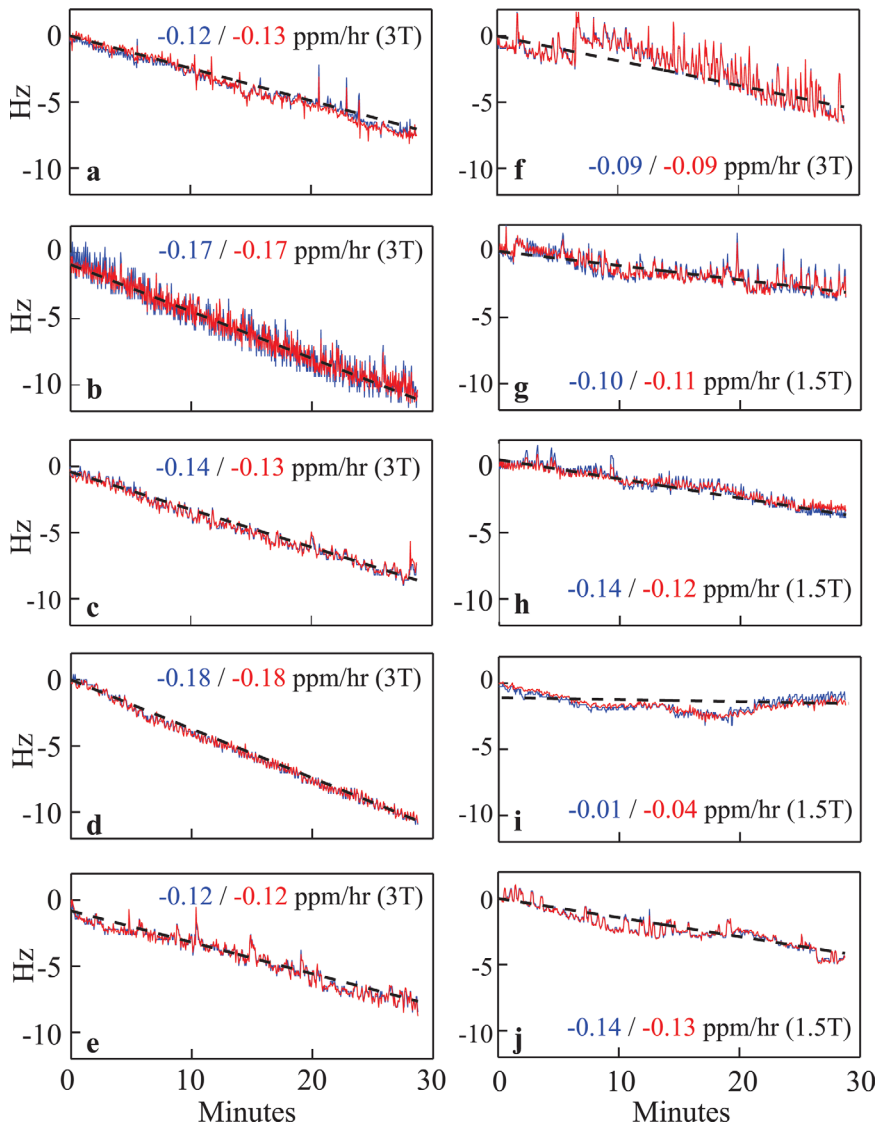


FIG. 3. In vivo drift-tracking in 10 healthy volunteers at 1.5 and 3 T, showing for each volunteer: (i) the instantaneous frequency as a function of scan time, as estimated from the position of the water peak from the interleaved scans (blue, solid); (ii) the weighted-least squares estimation (Eq. [11]) from just the first 21 points (10 ms) in each interleaved FID (red, solid); (iii) the linear fit (black, dashed) to the Fourier transformed (blue solid) data; (iv) The drift, in ppm/h, as calculated from both estimators (blue: Fourier transformed. red: weighted least squares). Note that all drifts are, to a good approximation, linear, and that the two estimators show excellent agreement.

“slow” y-axis (Fig. 5c–e) show distorted lineshapes, and benefit considerably from the drift correction. This is similar to the effects observed in the phantom before (Fig. 2d) and after (Fig. 2e) drift correction. In particular, the drift correction eliminated the spurious signal in the ventricles (gray arrow in Fig. 5e). Conversely, no striking improvements are observed when the voxel is surrounded by other voxels having a similar spin density (Fig. 5f). Here, the drift-induced spatial averaging implied by Eqs. [3] and [8] merely averages the voxel with similar adjacent voxels which do not modulate the signal appreciably; i.e., “the spatial average of a homogeneous medium is a homogeneous medium.”

## DISCUSSION

The spins’ resonant frequency always declines over time due to small resistive losses in any superconducting magnet. This drift is often disclosed in the magnet’s specification sheets at under 0.1 ppm/h, but this is often measured under no load and no gradient and shim activ-

ity. The drifts measured herein were mostly in the 0.1–0.2 ppm/h range for both 1.5 and 3.0 T magnets. Literature reports, summarized in Table 1, range from 0.03 up to 6.5 ppm/h and vary with magnet, field strength and sequence used, but most are approximately a few tenths of a ppm/h. A 0.1 ppm/h drift at 3 T would accrue about 6 Hz over 30 min, on the order of the voxels’ spectral linewidth, and hence, lead to non-negligible localization errors according to Eq. [9].

In contrast to single-voxel measurements, drift does not induce line broadening in phase-encoded CSI. Rather, the drift-induced phase and frequency uncertainties result in localization errors. Line broadening, however, can be observed as a consequence of the spatial averaging when the shim, spin density or relaxation change appreciably on the order of the spatial shift experienced by the PSF (e.g., Eq. [5] in 1D). For example, the lineshape in the voxel containing the spherical phantom appears broadened before correction (before: Fig. 2c vs. after: Fig. 2e): as the PSF shifts outside the voxel containing the phantom, the signal decays to zero on a time

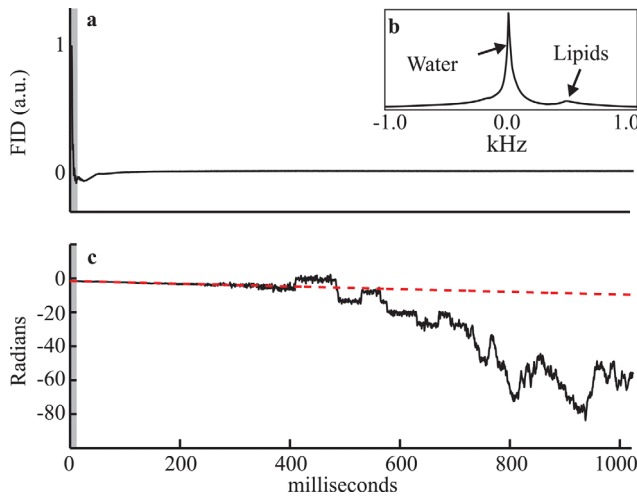


FIG. 4. A representative interleaved non-localized FID (out of  $24 \times 24 = 576$ ) from one of the volunteers. **a**: The real part of the FID, which decays quickly due to the short whole-head  $T_2^*$ . **b**: The whole-head spectrum in magnitude mode. Note the dominant water peak and the much smaller lipid peak. **c**: The phase of the FID (black, solid), superimposed on the fitted weighted least squares line (red, dashed). The slope of the line equals the instantaneous frequency (multiplied by  $2\pi$ ) during that particular scan. Only the first 10 ms (shaded) are used for fitting the line using Eq. [11]. Note how, for low SNR ( $\leq 3$ ) around ca. 350–400 ms, the phase unwrapping algorithm begins to fail as the noise in the phase domain becomes too large. [Color figure can be viewed in the online issue, which is available at [wileyonlinelibrary.com](http://wileyonlinelibrary.com).]

scale faster than the voxel's  $T_2^*$ , thus broadening (and slightly distorting) the lineshape. The exact effects will depend on the local environment of each voxel.

Several 3D CSI variants incorporate echo planar spectroscopic imaging (EPSI) modules to speed up the acquisition. The most common approach uses EPSI along one axis and phase-encoding along others (27), while others extend it to all three axes (28). When EPSI is used for one direction, the drift effects appear only along the two phase-encoded axes, in a similar manner as described so far (Eq. [3]). For example, for a 2D acquisition in the  $k_x$ - $k_y$  plane in which the  $k_x$ -axis is phase-encoded and EPSI is used for the  $k_y$ -axis, is the signal from the  $n$ th acquisition is:

$$s_n(t) = e^{2\pi i n \Delta \nu_{\text{scan}} t} \int_{-\infty}^{\infty} e^{2\pi i k_n x} \left[ \int_{-\infty}^{\infty} M_0(x, y) e^{2\pi i k_y(t) y} dy \right] dx \quad [15]$$

where  $\Delta \nu_{\text{scan}}$  is the change in the spins' resonance frequency between consecutive phase-encoded scans,  $k_n = -k_{\text{max}}/2 + n\Delta k$  ( $n = 0, 1, \dots, N-1$ ),  $\Delta k = \text{FOV}^{-1}$  and  $k_{\text{max}} = N \cdot \Delta k$ . Equation [15] is similar in form to Eq. [1], and the conclusions are identical. Because of the low in vivo SNR encountered, EPSI sequences need the same time as ordinary phase-encoded CSI (29), making them just as susceptible to drift effects. The effects of field drifts on a full volumetric 3D EPSI acquisition, in which all of  $k$ -space is acquired in a very short window of time, are of a different nature, and resemble those encountered in single-voxel MR spectroscopy (4): each scan acquires the entire spectrum, which drifts throughout acquisition.

Averaging the different spectra will then result in line broadening but no localization errors since localization is achieved in a single, fast ( $\sim 1$  s) volumetric scan of  $k$ -space, during which the effects of drift are negligible.

#### Drift Correction

The effects of any drift slow enough to be considered constant within a single scan can be corrected if the instantaneous spins' resonant frequency is known. The question, therefore, becomes one of instantaneous frequency estimation. The correction can then be done on the fly or retrospectively via post-processing. On-the-fly approaches are preferred since they address the drift-induced mismatch between the magnet's and RF's center frequencies, which can decrease the performance of water suppression and volume selection pulses. Henry et al. (4) use interleaved FIDs to adjust  $B_0$  in real time via a Z0 shim coil, not commonly found in human imagers. In contrast, Benner et al. (8) circumvent the need for specialized hardware by adjusting the receiver and transmitter center frequencies directly during an EPI-based DTI acquisition. To track the instantaneous frequency, the authors use the phase of the central point of  $k$ -space, which has a high signal to noise ratio and is acquired every TR. Although this works well for repeated single-scan acquisitions, such as fMRI (7,23) and DTI (8), which visit the central  $k$ -space point each TR, it is inappropriate for CSI in which the center of  $k$ -space is visited only once or at most a small number of times. Thus, regardless of whether a post-processing or real-time approach is taken, sequence and/or hardware probes are required to track the instantaneous frequency during CSI.

Hardware probes offer an excellent means for observing not only temporal but also spatial field variations (12), but require specialized hardware. The alternative is to interleave the pulse sequence with some form of reference scan, which is the approach taken by the majority of other publications dealing with field drift during CSI (4,11,14,15). For example, Ebel et al. used an EPSI-module for their reference scan on non-suppressed water, which afforded additional  $B_0$  correction capabilities, but requires fast-switching gradients and specialized post-processing expertise to implement. In Ref. 24, a localized navigator echo was incorporated for correcting for both field drift and motion artifacts, albeit at the cost of additional volume-selection RF pulses. The much simpler acquisition of a nonlocalized FID, used in the current paper, was also used in Ref. 4. Although this method does not correct spatial field variations, its appeal lies in its simplicity, robustness and minimal sequence modifications required.

The interleaved scans should be kept as short as possible for two reasons: (i) not to perturb TR or impose unnecessary restrictions on each scan's duration; (ii) to provide some immunity from the instantaneous frequency changes even on short,  $\sim 1$  s, time scales due to patient motion, respiration and blood flow. Figure 3 shows that, for a well-shimmed sample ( $\sim 20$ – $30$  Hz whole-head at 3 T), even a 10 ms acquisition is sufficient to obtain excellent (few tenths of a Hz) accuracy if the

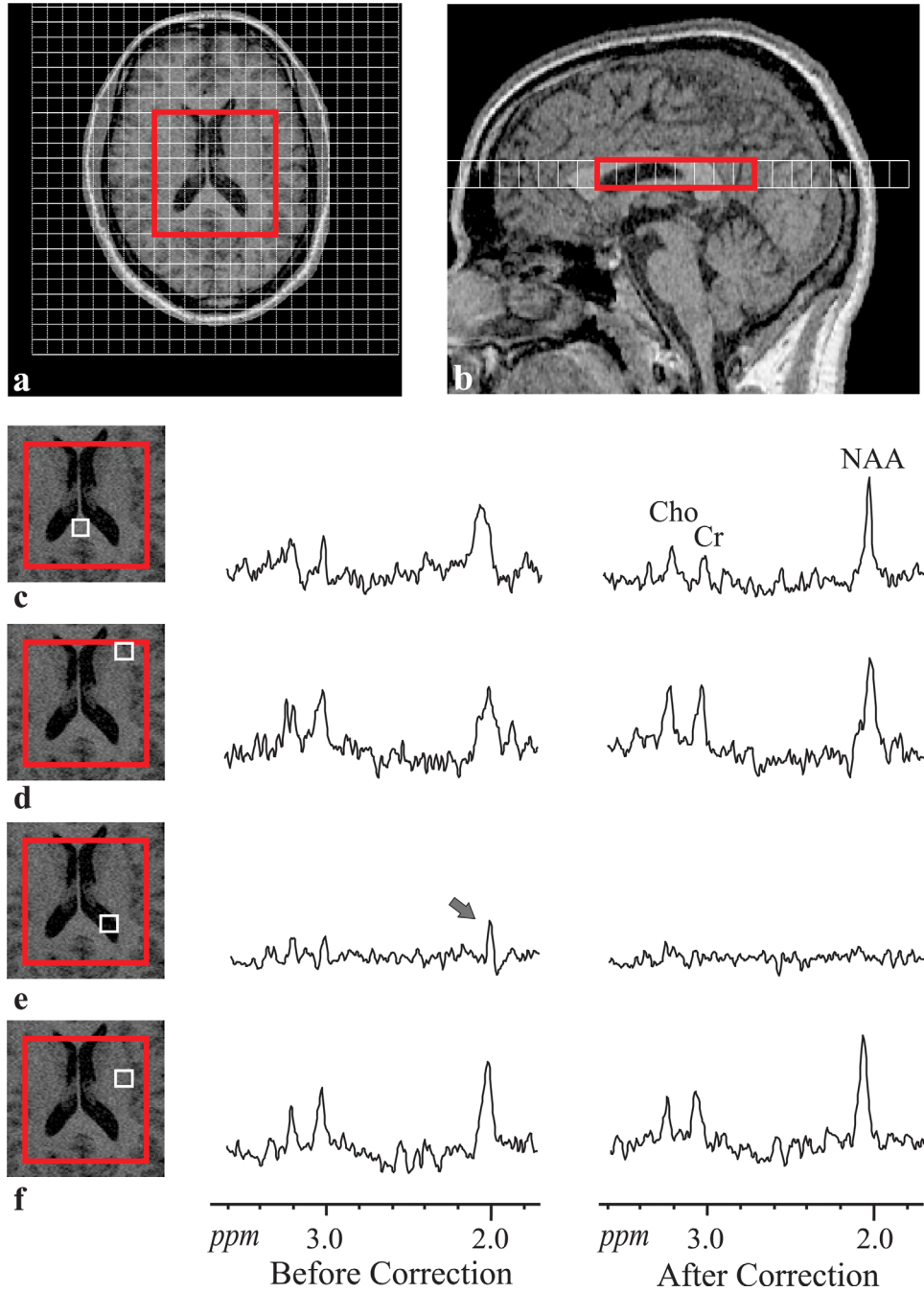


FIG. 5. Sample in vivo spectra from a volunteer. The corresponding drift curve is shown in Fig. 3d. **a** and **b**: VOI (red box) and FOV (white grid) placement on anatomical MPRAGE images. Spectra before and after drift correction are shown in **(c–f)**. Note that the voxels in **(c–e)** are positioned close to discontinuities in the spin density and, consequently, visibly benefit from the drift correction. In particular, note the elimination of the spurious NAA signal in the ventricles in **(e)**. Much less pronounced artifacts are observed in **(f)** due to the voxel’s homogeneous surroundings. [Color figure can be viewed in the online issue, which is available at [wileyonlinelibrary.com](http://wileyonlinelibrary.com).]

WLS estimator is used (Eq. [11]). Although this computation requires the SNR at each time point of the interleaved scans’ FIDs ( $\sigma_n$  in Eq. [11]), it is highly tolerant to estimation errors—any errors will merely give slightly different weight to different time points, increasing the standard deviation proportionally, but never beyond that of a non-WLS procedure.

**Drift Linearity**

On the time scales of a CSI experiment, the drifts encountered were predominantly linear (Fig. 3). This linearity is not necessary for correcting the drift’s effect.

However, it does serve to validate the theoretical effects analyzed in this article. The drift’s linearity is supported by the literature: Peters et. al. (22) reports a linear drift in a phantom, measured with a simple pulse-acquire over 25 min, modulated only by variations in the phantom’s temperature due to air conditioning variations, that are not expected in vivo. A  $\sim 0.5$  ppm/h drift was observed over 10 min due to heating of the passive shims in a PRESS sequence (4). An almost-linear drift of about 0.35 ppm/h, with a small quadratic component, was recorded in an EPSI acquisition (14). Therefore, when it is impossible to modify the sequence or hardware, the linear approximation is a useful first order

Table 1  
Literature Review of Typical Drift Magnitudes, Spanning a Wide Range of Manufacturers, Magnets, Fields, and Subjects

Ref.	$B_0$	Manufacturer	Drift (ppm/h)	Subject	Sequence
(22)	1.5 T	GE Signa	0.55	Phantom	Thermometry using spoiled gradient echo imaging
(4)	3 T	Bruker Avance	0.5	Human	PRESS interleaved with FID acquisition
(7), (23)	1.9 T	GE/Elscint Prestige	Not reported <sup>a</sup>	Human	EPI fMRI
(11)	1.5 T	Siemens Magnetom	0.05	Phantom	Multiple pulse-acquire before and after acquiring a CSI dataset
(6)	1.5 T	GE Signa Horizon	Sinusoidal <sup>b</sup>	Phantom	EPI fMRI
(24)	7 T	Bruker Biospec	0.03	Rat	PRESS interleaved with navigator scan
(13)	1.5 T	Siemens Sonata	1.49	Phantom	FLASH and SSFP
(14)	3 T	Siemens Trio	0.35	Human	EPSI interleaved with FID acquisition
(5)	4 T	Varian INOVA	0.85	Human	EPI fMRI
(25)	3 T	GE Signa	0.48	Human	Spiral EPI fMRI
(8)	1.5 T	Siemens Avanto	2.34	Human	DTI
(26)	3 T	Philips Achieva	6.5	Phantom	Multi gradient echo thermometry
(15)	3 T	Siemens Trio	0.03 <sup>c</sup>	Phantom	PRESS with interleaved FID acquisition

<sup>a</sup>The drift was shown to induce geometrical distortions in EPI of 2–3 voxels.

<sup>b</sup>A sinusoidal  $\pm 5$  Hz variation in  $B_0$  with a period of ca. 2 min was reported, attributed by the authors to a power line in the room.

<sup>c</sup>These drifts were observed following an intensive diffusion weighted EPI sequence. Prior to that, even smaller drifts (not exceeding 0.01 ppm/h) were observed.

correction: the user can measure the water's resonant frequency before and after the CSI experiment with (possibly) several acquisitions to average out physiological variations and correct for drift assuming linearity.

Non linear drift components can be observed depending on magnet quality and whether a high duty cycle sequence was run on the magnet prior to CSI as described in Ref. 15; such nonlinearities can persist for half an hour, depending on the amount of passive shim elements in the system. For a complete correction, the spins' instantaneous frequency must be tracked. Several suggestions have been made for tracking the temporal frequency changes, including interleaving reference scans and adjusting the  $Z_0$  gradient (4) or correcting in post-processing (15), using navigator echoes and centroids (7,24), introducing specialized field probes into the scanner (12), or using reference-less approaches which rely on multiple gradient echoes (26).

As evident from Fig. 3, the instantaneous frequency displays a noisy component which cannot be attributed solely to the estimator's variance; this "noise," the source of which is most probably physiological, is characterized by frequency variations on the order of TR. Before correction is attempted it is advised that a polynomial fit or similar smoothing procedure be applied, to minimize the effects of frequency shifts within a single TR.

Localization errors are particularly insidious in vivo in the brain, where small changes in metabolite levels are sought, as they are difficult to detect by visual inspection: since the effect of a linear drift is to spatially average adjacent voxels (Eq. [3]), and since the brain's metabolite levels are fairly spatially homogeneous, the drift's effects can be subtle (Fig. 5f). However, that is not to say it is unimportant: drift will average spin density/shim/linewidth variations between, e.g., healthy and diseased tissue, thus reducing both specificity and sensitivity. Voxels close to the ventricles and the VOI's edges also benefit from proper drift correction (Fig. 5c–e).

## CONCLUSIONS

All superconducting magnets suffer a drift. In real-world scenarios, this drift has a strong linear component (ca. 0.1 ppm/h in vivo, as shown herein) and introduces localization errors in CSI protocols, which can become substantial for long acquisition times. Correcting for it is straightforward if the instantaneous resonant frequency can be estimated and smoothed. Interleaved FIDs offer a simple, easily implemented and low SAR solution for doing so; fitting the FID's phase using WLS provides high accuracy and precision, while keeping the duration of the interleaved FIDs to a minimum (ca. 10 ms).

## REFERENCES

- Henkelman RM, Bronskill MJ. Artifacts in magnetic resonance imaging. *Rev Magn Reson Med* 1987;2:1–126.
- Smith AM, Lewis BK, Ruttimann UE, Ye FQ, Sinnwell TM, Yang Y, Duyn JH, Frank JA. Investigation of low frequency drift in fMRI signal. *Neuroimage* 1999;9:526–533.
- De Poorter J, De Wagter C, De Deene Y, Thomsen C, Stahlberg F, Achten E. The proton-resonance-frequency-shift method compared with molecular diffusion for quantitative measurement of two-dimensional time-dependent temperature distribution in a phantom. *J Magn Reson B* 1994;103:234–241.
- Henry P-G, Van De Moortele P-F, Giacomini E, Nauerth A, Bloch G. Field-frequency locked in vivo proton MRS on a whole-body spectrometer. *Magn Reson Med* 1999;42:636–642.
- Foerster BU, Tomasi D, Caparelli EC. Magnetic field shift due to mechanical vibration in functional magnetic resonance imaging. *Magn Reson Med* 2005;54:1261–1267.
- Durand E, Van De Moortele P-F, Pachot-Clouard M, Le Bihan D. Artifact due to  $B_0$  fluctuations in fMRI: correction using the k-space central line. *Magn Reson Med* 2001;46:198–201.
- Liu H-L, Kochunov PV, Lancaster JL, Fox PT, Gao J-H. Comparison of navigator echo and centroid corrections of image displacement induced by static magnetic field drift on echo planar functional MRI. *J Magn Reson Imaging* 2001;13:308–312.
- Benner T, van der Kouwe AJW, Kirsch JE, Sorensen AG. Real-time RF pulse adjustment for  $B_0$  drift correction. *Magn Reson Med* 2006; 56:204–209.

9. El-Sharkawy AM, Schar M, Bottomley PA, Atalar E. Monitoring and correcting spatio-temporal variations of the MR scanner's static magnetic field. *Magn Reson Mater Phys Biol Med* 2006;19:223–236.
10. Zaitsev M, Speck O, Henning J, Buchert M. Single-voxel MRS with prospective motion correction and retrospective frequency correction. *NMR Biomed* 2010;23:325–332.
11. Schmidt O, Widmaier S, Bunse M, Jung WI, Dietze GJ, Lutz O. Artifacts in CSI-measurements caused by the drift of the static magnetic field. *Magn Reson Mater Phys Biol Med* 2000;10:167–170.
12. Barmet C, De Zanche N, Pruessmann KP. Spatiotemporal magnetic field monitoring for MR. *Magn Reson Med* 2008;60:187–197.
13. Scheffler K. Fast frequency mapping with balanced SSFP: theory and application to proton-resonance frequency shift thermometry. *Magn Reson Med* 2004;51:1205–1211.
14. Ebel A, Maudsley AA. Detection and correction of frequency instabilities for volumetric 1H echo-planar spectroscopic imaging. *Magn Reson Med* 2005;53:465–469.
15. Lange T, Zaitsev M, Buechert M. Correction of frequency drifts induced by gradient heating in 1H spectra using interleaved reference spectroscopy. *J Magn Reson Imaging* 2011;33:748–754.
16. Goelman G, Liu S, Hess D, Gonen O. Optimizing the efficiency of high-field multivoxel spectroscopic imaging by multiplexing in space and time. *Magn Reson Med* 2006;56:34–40.
17. De Graaf RA, Brown PB, McIntyre S, Rothman DL, Nixon TW. Dynamic shim updating (DSU) for multislice signal acquisition. *Magn Reson Med* 2003;49:409–416.
18. Brown TR, Kincaid BM, Ugurbil K. NMR Chemical Shift Imaging in Three Dimensions. *Proc Natl Acad Sci* 1982;79:3523–3526.
19. Gudbjartsson H, Patz S. The rician distribution of noisy MRI data. *Magn Reson Med* 1995;34:910–914.
20. Rao CR, Toutenburg H, Fieger A, Heumann C. Linear models: least squares and alternatives. Springer series in statistics, 2nd ed. Berlin: Springer-Verlag; 1999. pp 109–112.
21. Hu J, Javaid T, Arias-Mendoza F, Liu Z, McNamara R, Brown TR. A fast, reliable, automatic shimming procedure using 1H chemical-shift-imaging spectroscopy. *J Magn Reson B* 1995;108:213–219.
22. Peters RD, Hinks S, Henkelman RM. Ex vivo tissue-type independence in proton-resonance frequency shift MR thermometry. *Magn Reson Med* 1998;40:454–459.
23. Kochunov PV, Liu H-L, Andrews T, Gao J-H, Fox PT, Lancaster JL. A B0 shift correction method based on edge RMS reduction for EPI fMRI. *J Magn Reson Imaging* 2000;12:956–959.
24. Thiel T, Czisch M, Elbel GK, Henning J. Phase coherent averaging in magnetic resonance spectroscopy using interleaved navigator scans: compensation of motion artifacts and magnetic field instabilities. *Magn Reson Med* 2002;47:1077–1082.
25. Sutton B, Noll D, Fessler J. Dynamic field map estimation using a spiral-in/spiral-out acquisition. *Magn Reson Med* 2004;51:1194–1204.
26. Sprinkhuizen SM, Bakker CJG, Bartels LW. Absolute MR thermometry using time-domain analysis of multi-gradient-echo magnitude images. *Magn Reson Med* 2010;64:239–248.
27. Posse S, DeCarli C, Le Bihan D. Three-dimensional echo-planar MR spectroscopic imaging at short echo times in the human brain. *Radiology* 1994;192:733–738.
28. Adalsteinsson E, Irarrazabal P, Topp S, Meyer C, Macovski A, Spielman DM. Volumetric spectroscopic imaging with spiral-based k-space trajectories. *Magn Reson Med* 1998;39:889–898.
29. Pohmann R, von Kienlin M, Haase A. Theoretical evaluation and comparison of fast chemical shift imaging methods. *J Magn Reson* 1997;129:145–160.